Liu *et al. eLight* (2026) 6:18
https://doi.org/10.1186/s43593-026-00132-1

elight.springeropen.com

RESEARCH ARTICLE

Open Access

Broadband coloured skyrmions generated by on-chip ferroelectric spherulites

Yuanfeng Liu[1], Liuhao Zhu[2,3], Xi Xie[3], Haoran Zhang[3,4], Weibo Gao[3,4], Bing Gu[2], Youcheng Xu[1], Le Zhou[5], Yongzheng Wen[1], Jingbo Sun[1*], Yijie Shen[3,4*] and Ji Zhou[1*]

Abstract

Optical skyrmions, particle-like topological textures of light with resilience to perturbation, hold great promise for next-generation robust information carriers. Recent advances have enabled their efficient generation and modulation in both classical and quantum regimes via artificial nanostructures with certain topological landscapes. However, existing studies are largely confined to (quasi)monochromatic domain, because the resonance-based linear and nonlinear light-matter interactions are constrained by narrowband response and strong spectral dispersion. Therefore, the exploration of coloured and white light skyrmions is virtually zero, blocking their extension to broadband information technologies. Here, we present an ultra-compact micro-generator that generates ultra-broadband coloured skyrmions from a natural ferroelectric spherulite crystal through the combined action of the photonic spin-orbital coupling and optical focusing. This approach circumvents the resonance effects intrinsic to artificially nanostructured optical systems. The resulting polychromatic skyrmions cover the entire visible spectral range and can propagate over an appreciable distance in free space. Their topological textures can be continually modulated by tuning the polarization of the incident beam, enabling switching among multiple topologies, such as skyrmions, biskyrmions, and quadrumerons. Furthermore, we reported the experimental evidence of spontaneous parametric down conversion process occurring within the ferroelectric spherulite, which implies the possibility to generate the correlated topological quantum states in further research. These distinctive features will revolutionize modern informatic applications spanning optical communication, data storage, and topological photonic devices.

1 Introduction

Skyrmions, with promising topological stability, describe specific particle-like topological spin textures of physical fields [1]. Classical and notable physical systems with skyrmions configurations are liquid crystals [2–4], ferroelectric [5–7] or magnetic domains [8, 9], quantum Hall systems [10], and Bose–Einstein condensates [11], etc., which show great potentials in empowering high information storage capacities [12–15], but are generally localized in matter, which challenges information transfer capacities. In comparison, optical skyrmions with flying and topological stability merits [16–19] are emerging, as promising candidate towards data transfer over a long distance [16, 20–22]. The pioneering work in generating optical skyrmions started from the electric field of local evanescent waves [23] and the spin field in confined

*Correspondence:
Jingbo Sun
jingbosun@tsinghua.edu.cn
Yijie Shen
yijie.shen@ntu.edu.sg
Ji Zhou
zhouji@tsinghua.edu.cn
[1] State Key Laboratory of New Ceramic Materials, School of Materials Science and Engineering, Tsinghua University, Beijing 100084, China
[2] School of Electronic Science & Engineering, Southeast University, Nanjing 211189, China
[3] Centre for Disruptive Photonic Technologies, School of Physical and Mathematical Sciences, Nanyang Technological University, Singapore 637371, Singapore
[4] School of Electrical and Electronic Engineering, Nanyang Technological University, Singapore 639798, Singapore
[5] Department of Physics, Colorado School of Mines, Illinois, St, Golden 1523, USA

surface plasmon polaritons [24]. Later, optical skyrmions are extended to the free space and to more diverse configurations [20, 25–27], including Stokes vectors [28–30], magnetic vectors [31], pseudospins [32], energy flows [33], crossing from classical to quantum regime [28, 34]. The intense studies on optical skyrmions are valuable for both fundamental researches [35–37], especially the topological photonics and structured light regarding to the topological features and potential applications in displacement sensing [38], magnetic domain imaging [39, 40], integer arithmetic [41], optical communication, and information storage, where the wideband capability of the skyrmions generation is essential. Although recent advances have enabled their efficient generation and modulation in classical and quantum regimes, all optical skyrmions demonstrated so far are largely limited in monochromatic or narrowband domains. To date, the direct generation of polychromatic coloured wideband skyrmions in the entire visible spectrum has not yet been experimentally achieved, blocking their extension to broadband information technologies.

To unlock broadband skyrmion-based informatics, another vital concern in the practice is the realization of ultra-compact integrated skyrmion generators on chip, rather than the constructed optical setups on an optical table in lab (see the optical path using spatial light modulators [42, 43]). Recently, the development of integrated generators for optical skyrmions, e.g. the metasurfaces [44], microrings [30], photonic crystal slabs [45], extended q-plate [46], and microcavity [28], has motivated the emerging practical informatics applications [20]. At present, such schemes operate solely for monochromatic skyrmionic beams. This restriction arises from resonance-based linear and nonlinear light-matter interactions in existing skyrmion optical systems, which exhibit pronounced spectral dispersion [47]. On the other hand, the devices require the micro-nano optical elements consisted of fine but sophisticated nanostructures, which, however, are always challenged by fine nanofabrication techniques of high cost. The simultaneous breakdown of the bandwidth barrier and nanofabrication constraint in optical skyrmion generation therefore demands a paradigm shift that circumvents the resonance effects intrinsic to artificial nanostructured optical systems by co-designing innovative integrated photonic devices alongside their material realization.

Here, we demonstrate the robust on-chip micro-generation of coloured optical skyrmions across the entire visible spectrum through a non-resonance optical system, that is using a ferroelectric spherulite with inherent circular anisotropy and dome-shaped geometry, which can be obtained through crystallization. By leveraging spin-orbital (SO) coupling [48] and focusing effects of the spherulite, the Stokes vectors featuring skyrmionic topologies including skyrmions, biskyrmions, and quadrumerons can be generated through the superposition of beams in orthogonal polarizations while with certain spin or orbital angular momentum (SAM or OAM) spatial distribution in the entire visible range. The generated skyrmions are shown to maintain a stable propagation of 7 Rayleigh lengths in free space. Moreover, the vortex ferroelectric domain in the spherulite breaks the symmetry in polarity and thus enables the natural second-order nonlinearity, which are used to generate photon pairs in a spontaneous parametric down-conversion (SPDC) process [49–52] and thus promises the potential skyrmion entangling. Our work provides a powerful photonic platform for manipulating topological photon states in the wide spectral range across the classical and quantum regimes and sheds light on the skyrmions based technologies by driving breakthroughs in broadband information transfer and high-dimensional classical and quantum communications [53].

2 Results

2.1 Design principles

A spherulite refers to the material featuring circular crystalline structure, and thus usually exhibits circular anisotropy in optics. In our work, the ferroelectric spherulite is comprised of polar molecules arranged in an azimuthal way, as shown in Fig. 1a. This molecular dipole configuration forms through a thermally driven self-assembly process, governed by the minimization of the system's free energy, which involves the interplay of elastic energy, surface anchoring, and polar electric field coupling [54]. This bottom-up process ensures molecular-level uniformity in light-matter interactions. Under the scanning electron microscope, the spherulite material is in a dome shape located on a glass substrate. The uniaxial anisotropy of the polar molecules makes the entire spherulite exhibits the circular anisotropy described by: n_r and n_θ, representing the refractive indices along radial and azimuthal orientations. Such a spherulite can bring in both the spin-orbital angular momentum coupling due to the special anisotropy and a focusing functionality, ultimately generating a beam with skyrmionic topology in Stokes vector polarization.

Assuming a Gaussian beam with right circular polarization (RCP) is incident on the spherulite from the substrate side, as shown in Fig. 1a. At the periphery region of the dome structure, the thickness is negligible and thus the beam passing through this region can be considered as no change in polarization but just bent to the foci due to the parabolic-like transmission phase distribution (Fig. S1). Detailed intensity evolution along the propagating direction can be found in Fig. S9. At the central region,

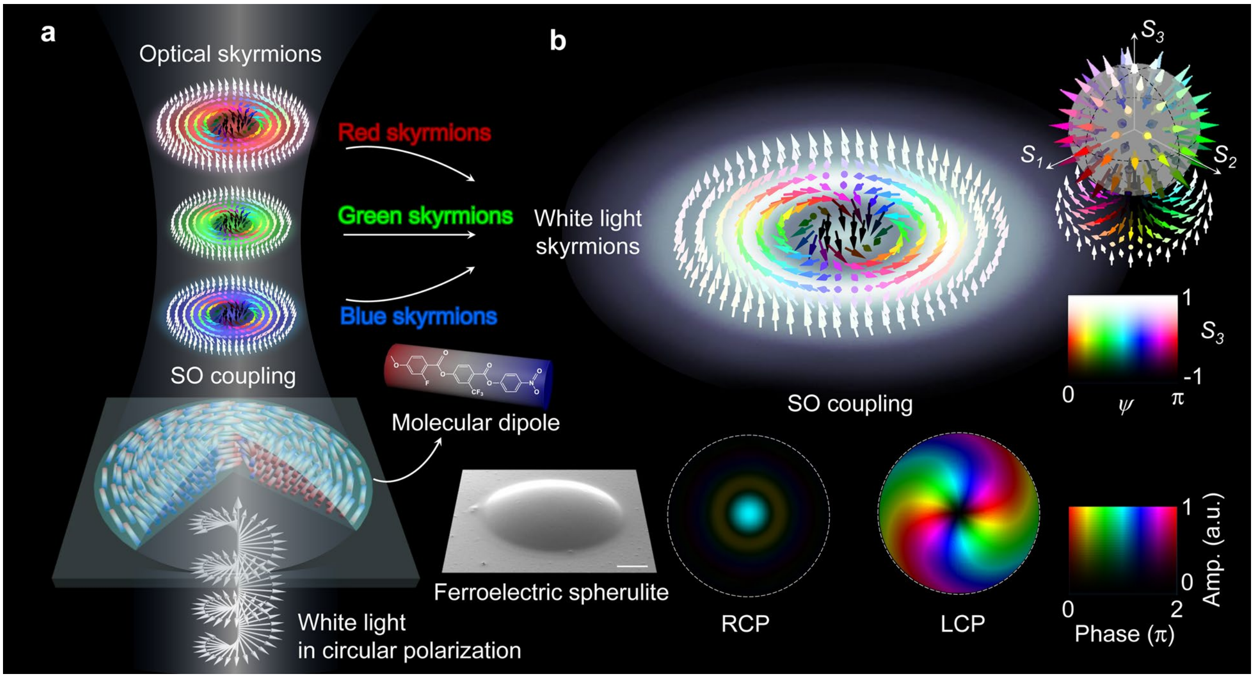

Fig. 1 Conceptual schematic of white light skyrmions generation from a single dome-shaped ferroelectric spherulite. **a** Generation schematics of white light skyrmions from one single ferroelectric spherulite. The dome-shaped spherulite was consisted of azimuthally oriented rodlike polar molecules of the uniaxial anisotropy, showing the rotation symmetry in both geometry and optical properties. The input beam of RCP experienced SO coupling and was subsequently focused by the dome-shaped ferroelectric spherulite to form Stokes skyrmionic topologies in the far field. In the case of white light incidence, skyrmionic topologies were formed at each wavelength, taking red skyrmions, green skyrmions, and blue skyrmions as examples. Inset: scanning electron microscope image of the fabricated spherulite. The scalebar of the scanning electron microscope image is 5 μm. **b** Texture and synthesis of white light optical skyrmions. The LCP with $LG_{0,-2}$ mode and RCP with $LG_{0,0}$ mode were robustly formed in the far field due to the SO coupling effects in the case of RCP incidence. Mapping such Stokes distribution to a Poincaré sphere, it exhibits the topological feature of a quasi-particle. In the bottom panel in **b**, the colour (lightness) represents the phase (intensity) of the complex fields of the LCP and RCP. In **a** and the top panel of **b**, the hue of the vector arrows represents different in-plane components of the Stokes vectors, and the lightness of the vector arrows corresponds to out-of-plane components of the Stokes vectors. Amp., amplitude

the thickness together with the circular anisotropy may result in a strong polarization modulation due to the phase delay $\Delta\phi$ between the radial and azimuthal E field components (Fig. S1). Once the phase delay is π, the spin of the incident beam is flipped and meanwhile OAMs are loaded, resulting in a left circular polarization (LCP) of topological charge −2. Such a transformed optical vortex beam is also focused to the same foci, whose singularity is filled by the RCP from the periphery region (Fig. S2 and S9). Such a synthesized beam fulfills the condition of constructing a skyrmionic beam, which is the superposition of the two beams of orthogonal polarization states ($|e_1\rangle, |e_2\rangle$), as expressed in Eq. (1) [55]:

$$|\psi\rangle = |l_1\rangle|e_1\rangle + e^{-i\Delta\varphi}|l_2\rangle|e_2\rangle \quad (1)$$

in which l_1 and l_2 indicate the carried OAM, namely the topological charges. In our case, ($|e_1\rangle, |e_2\rangle$) denote the left and right circular polarization, respectively, and $l_1 = -2$, $l_2 = 0$ represent the superposition of $LG_{0,-2}$ and $LG_{0,0}$ modes, which generates polarization states that span the entire Poincaré sphere. We visualized the polarization textures of the generated skyrmions using normalized Stokes vectors in 2D, as shown in Fig. 1b. The Stokes vector fields cover the Poincaré sphere twice, satisfying the condition for a Skyrme number of $N_{sk} = -2$. Through the same way, an LCP beam can be used to generate a skyrmion with $N_{sk} = 2$, as explained in Fig. S1. The resultant spatially-varying vector pattern will fulfill a skyrmion mapping (Fig. 1b), i.e., the mapping of all polarization states from a parametric sphere to a localized transversal plane.

The dispersion of the spherulite is rather weak, and thus a relatively fix $\Delta n = 0.102 \pm 0.008$ in the whole visible range, as shown in Fig. S10 in supplementary information. Therefore, white skyrmions can be generated by one single spherulite under a circularly polarized white light illumination.

2.2 White light skyrmions generation

As we have discussed above, in principle, the generation of the LCP vortex beam of topological charge −2 requires a very strict thickness under the certain anisotropy, so that the spherulite can bring in the right phase delay. In reality, such a system has a very strong tolerance. To explore this, we calculate N_{sk} of the polychromatic skyrmions generated from different geometric scales through numerical simulations. Due to the crystallization and the surface tension, all the spherulites, despite different radii, have the same contact angle of 35°, which means that the height h of the dome is locked with the radius r, determined by the relation $h = r[\csc(\theta) - \cot(\theta)] = 0.31r$. The calculated results are shown in Fig. 2b, which shows that in a relatively wide range of the spherulite size in radius, the generated skyrmion number $|N_{sk}|$ is larger than 1.9, close to the ideal case of 2, under the illumination of either LCP or RCP. By converting the r into h, we find that if the effective phase delay at the central part of the spherulite is $\pi \pm 0.13\pi$, a high quality of skyrmion with $|N_{sk}| > 1.9$ can also be accomplished at each wavelength in the visible range, which in turn implies the robustness of the skyrmion.

According to Fig. 2b, a spherulite with a radius of 7 μm can be used to generate skyrmion textures of $|N_{sk}| > 1.9$ throughout the visible spectrum simultaneously. To test this, we fabricate the spherulite on such a size specially. The optical measurement set-up that can extract Stokes components (S_1, S_2, S_3) of the beam at the focal spot after the spherulite is presented in Fig. S3. The source is a supercontinuum laser that enables us to perform the measurement in the spectrum ranging from 450–785 nm. As shown in Fig. 2c, the Stokes polarization distribution of the generated skyrmions at each wavelength maintains a high consistency. Especially, the extracted Stokes components (S_1, S_2, S_3) at the two ends in the visible spectrum (450 nm, 750 nm) are shown in Fig. 2d, e. Other measurement results can be found in Fig. S4 and Fig. S7. The skyrmion numbers $|N_{sk}|$ calculated based on these experimental results are all larger than 1.9 and show excellent agreement with analytical calculations, which demonstrates the high tolerance on material's dispersion and thus the feasibility of generating white light skyrmions.

2.3 Longitudinal evolution of skyrmions

The longitudinal propagation behavior is related to the focusing ability of the spherulite. To explore this, we perform a ray tracing measurement on the beam at 530 nm out of the spherulite, by capturing its intensity profile as

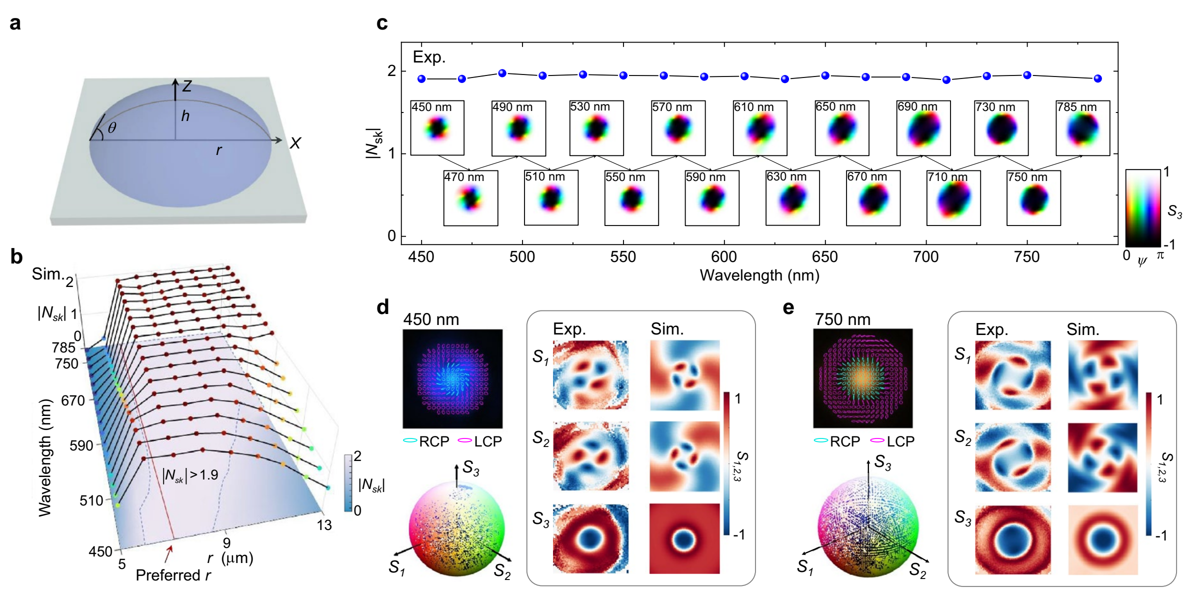

Fig. 2 Wideband generation of Stokes skyrmions. **a** Schematics of a dome-shaped ferroelectric spherulite with the constant contact angle of 35°, the radius of r, and the central height of h. **b** Simulated results of the variation of Skyrme numbers respect to different radii of the spherulite and different wavelengths within 450–785 nm. The dashed boundary area shows the parameter space where $|N_{sk}|$ is larger than 1.9. The preferred radius is also noted using an arrow to allow the $|N_{sk}| > 1.9$ from 450–785 nm. **c** Experimental results of the Skyrme numbers at different wavelengths tested from a single spherulite whose structural footprint corresponds to the radius of 7 μm, as pointed in **b**. Inset: Stokes skyrmion textures at different wavelengths. **d** Left top: intensity and polarization textures at 450 nm. Left bottom: polarization states rendered on the unit Poincaré sphere. Right: extracted Stokes components in the experiment and simulation. **e** Left top: intensity and polarization textures at 750 nm. Left bottom: polarization states rendered on the unit Poincaré sphere. Right: extracted Stokes components in the experiment and simulation. The detailed Stokes skyrmions analysis at other representative wavelengths can be found in supplementary information

well as the Stokes polarization distributions across the cross-section of the beam with a step of 1 μm along its propagation direction and the results are shown in Fig. 3. As we have discussed above, a skyrmion is formed by the overlap of the two beams $LG_{0,0}$ and $LG_{0,2}$, which should occur around the focal spot due to the convex shape of the spherulite. Therefore, before the foci, the skyrmion has not yet well prepared and the N_{sk} is deviated from the ideal number of 2. Approaching to the focal spot, N_{sk} is quite close to 2. The theoretical numerical aperture (NA) is around 0.4, which enables a rather long depth of focus, and thus a long propagation of the skyrmion. Despite longitudinal polarization evolution and divergence during free-space propagation, the skyrmion textures exhibit high topological stability, with the nearly designed skyrmion number ($|N_{sk}| > 1.9$) at a distance of 28 μm, about 7 Rayleigh lengths (Fig. 3) that we can measure. At even further distance, the topological feature of the skyrmion should be still well maintained, however, the beam's intensity is quite weak due to the divergence. Theoretically, the beam can maintain its skyrmionic topology to infinite. The polarization textures at the cross-section along the propagation are also studied and the results are shown in Fig. S6, which shows the robust topological feature over appreciable propagation distance. Such excellent stability in the topological feature as well as the diffraction resilience implies the potential applications in optical tweezers or on-chip optical communication.

2.4 Tunability of the topological textures

Next, we expanded the family of optical quasiparticles from the fundamental skyrmion to its counterparts with more diverse topological textures, synthesized with other orthogonal configurations, with a more general form of Eq. (2) [46, 55–57]:

$$|\psi\rangle = \sum(\alpha_{Ln}|l_1\rangle|e_1\rangle + e^{-i\Delta\varphi}\alpha_{Rn}|l_2\rangle|e_2\rangle) \quad (2)$$

where the parameters α_{Ln} and α_{Rn} are functions of r and θ, which can further adjust the Stokes vectors topology in space [55, 58]. According to Eq. (2), topological quasiparticles of different types can be obtained through spherulites by taking its advantage of circular anisotropy.

Specifically, for the incident polarization at the pole in the Poincaré sphere (see Fig. 4a), the Stokes texture is in a skyrmionic configuration. By utilizing a linear polarized beam as the incidence, polarization states are maintained along the North (N)–South (S) and East (E)–West (W) directions since the polarization is either parallel or normal to the local optical axis (OA), showing a red cross at the Stokes polarization distribution. Along the Northeast (NE)–Southwest (SW) and the Northwest (NW)–Southeast (SE) directions, the angles between the polarization and the local OA is ± 45°. At the region that is roughly $r/2$ away from the center, a π/2 phase difference could be induced between the local E_x and E_y, enabling the LCP or RCP, indicated by the black and white spots at the Stokes polarization

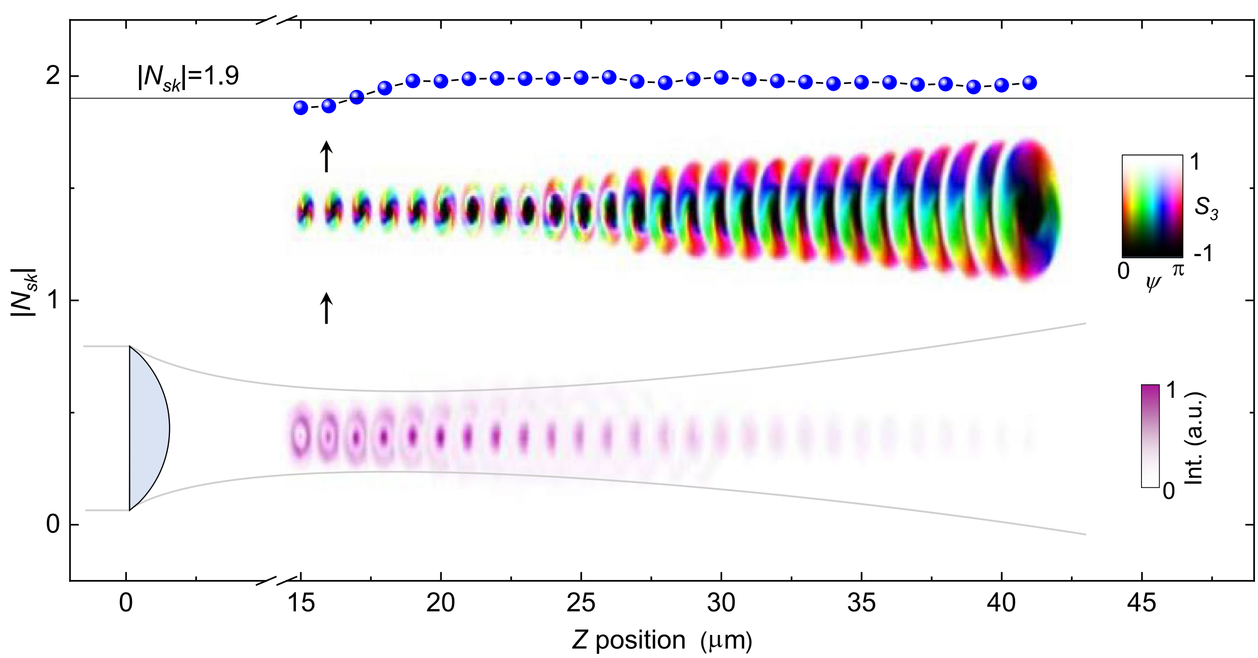

Fig. 3 Skyrmion texture evolution at different positions when propagating. The lower panel shows the intensity evolution. The upper panel shows the corresponding skyrmion textures. The Skyrme numbers are also plotted with blue circles. Int., intensity

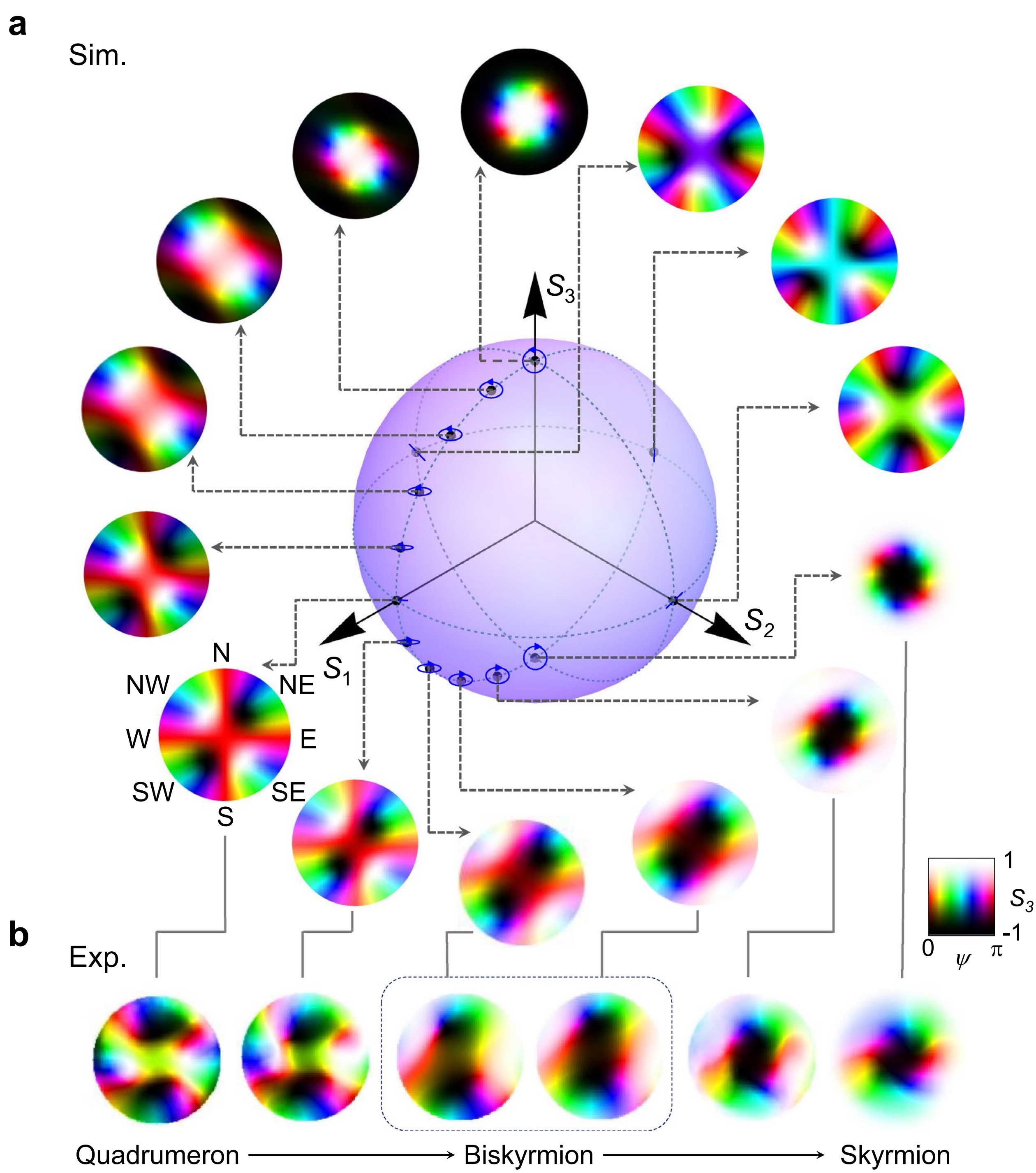

Fig. 4 Tuning Stokes vector textures by controlling the incident polarization. **a** Simulation results of the optical Stokes vector textures generated from different polarization incidences in the Poincaré sphere. **b** Stokes vector textures of the experimentally generated representative optical topological quasiparticles, including quadrumeron, biskyrmion, and skyrmion

distribution. Further away from the center, the thickness of the spherulite is decreasing, and thus elliptical polarizations are induced with different ellipticity, as indicated by the rainbow colour surrounded each black or white spots. Overall, a quadrumeron configuration emerges.

Even if the incident polarization is elliptical, which is relatively uncertain compared to the linear or circular cases, due to the circular anisotropy of the spherulite that contains OA of all orientations, along the azimuthal direction, one can always find the right orientation that can fully cancel the phase delay between E_x and E_y, which converts the incident elliptical polarization into the pure linear polarization. At other orientations where phase delay is well compensated so that the elliptical polarization transferred into the circular polarizations. However, due to the elliptical property, these featured polarizations can only appear twice along one circle on the spherulite and thus induce biskyrmion topologies at the Stokes polarization distribution. The experimental results are in good agreement with the simulations, as shown in Fig. 4b. It is noticeable that the Stokes vectors in the experiment are relatively rotated compared with simulations, which could be associated with the longitudinal polarization evolution effect when the beam is propagating in free space. Nevertheless, the generated topologies are still well protected and merely determined by the polarization state of the incident beam.

2.5 Exploration of the parametric photon pair generation

Besides the optical anisotropy in a linear optical realm resulted by the azimuthally arranged molecules, the ferroelectric feature from the vortex polarity order also endows intriguing second-order nonlinear optical responses. The previous study has demonstrated that this material possesses a relatively high second-order nonlinear coefficient [59, 60], as calibrated through the process of broadband second-harmonic generation (SHG). Once SPDC, the reverse process of SHG is observed, implying that the ferroelectric spherulite structure could enable skyrmion applications in the quantum regime [61]. Unlike the direct generation of on-demand single-photon skyrmions [28], SPDC produces photon pairs [62], thereby allowing the realization of skyrmions in the form of either heralded single photons or entangled photon pairs [63, 64]. The nonlinear optical characterizations are based on a back-reflection setup, and the spherulite is prepared on a SiO_2/Ag/SiO_2 substrate, where the intermediate Ag layer is used as the reflection layer for the signal collection, as shown in Fig. 5. To minimize fluorescence effects, a continuous-wave pump laser with a wavelength of 785 nm is employed, yielding SPDC photon pairs at approximately 1570 nm. Superconducting nanowire single-photon detectors (SPSNDs), together

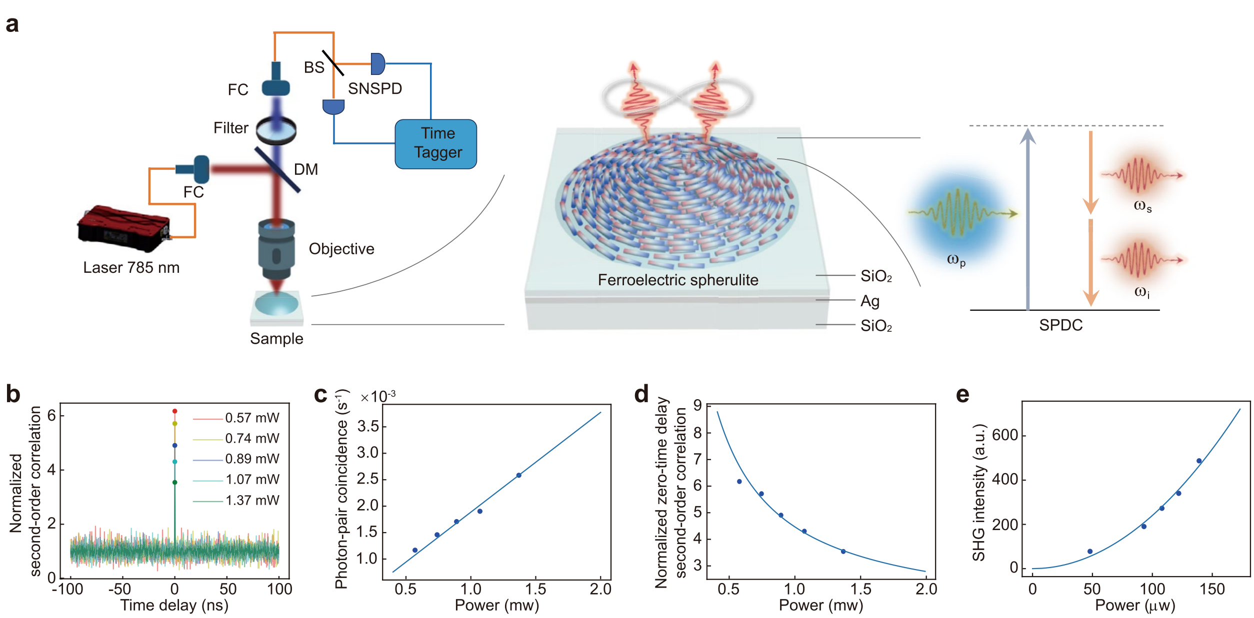

Fig. 5 SPDC and SHG characterizations of the ferroelectric spherulite. **a** Left panel: illustration of the optical setup for SPDC experiment of the ferroelectric spherulite. The pump beam is from a continuous-wave laser with the central wavelength at 785 nm. FC, fiber coupler; BS, beam splitter; DM, dichroic mirror; SNSPD, superconducting nanowire single-photon detector; Time Tagger, streaming time-to-digital converter. Middle panel: the ferroelectric spherulite sample for SPDC tests is formed on a SiO_2/Ag/SiO_2 layered substrate. Right panel: illustration of the SPDC process, in which a high-energy pump photon with the frequency of ω_p converts into a pair of low-energy photons consisting of a signal photon and an idler photon. **b** Normalized second-order correlation functions measured from the sample under different pump powers. **c** Dependence of the photon-pair coincidence rate on pump power. **d** Dependence of normalized second-order correlation function at zero-time delay on pump power. **e** Dependence of SHG intensity on pump power

with low-jitter streaming time-to-digital converters, are employed to record the arrival times of the infrared photons in the Hanbury Brown–Twiss second-order interference experiment. The normalized second-order correlation functions $g^{(2)}(\tau)$ measured from the sample under different pump powers are presented in Fig. 5b. The value of $g^{(2)}(0)$ decreases with increasing pump power, since both photon-pair generation and background scale linearly with pump power, leading to a reduced ratio of photon-pair coincidences to random coincidences. After correcting for dark counts, Fig. 5c shows a linear dependence of photon-pair coincidences on the pump power, while Fig. 5d illustrates that $g^{(2)}(0)$ decreases with pump power following a relation of $g^{(2)}(0) = \frac{a}{p} + 1$. In contrast, the SHG signal power exhibits a quadratic dependence on the pump power, as shown in Fig. 5e. The above results indicate that the ferroelectric spherulite is a promising SPDC sources with ultracompact and integrable potentials towards chip-based photonic quantum circuits. Despite that the current evidence is insufficient to confirm that the detected SPDC photons correspond to quantum skyrmions, it implies that the fusion of the capabilities in generating photon-pairs and white light skyrmions by using a single ferroelectric spherulite may stimulate the research on the robust generation of quantum skyrmions in a compact platform.

3 Discussions

This work demonstrates a new paradigm for generating optical skyrmions via nanostructured ferroelectric spherulites through self-assembly, with the core advantage of circumventing the reliance on resonance-based photonic systems, namely, artificial nanostructures that require complex and costly nanofabrication techniques. Our proposed photonic platform achieves significant breakthroughs in two key dimensions: unprecedented operational bandwidth and flexible tunability. Together, these features open up new possibilities for structured photonics and its applications.

The most significant and well-supported contribution of this work is its ultra-broadband capability. The experimental results clearly show that a single spherulite can efficiently generate topologically stable skyrmions across the entire visible spectrum (450–785 nm). This property fundamentally overcomes the narrowband limitations inherent to current mainstream technologies, such as metasurfaces and microcavity resonators [30, 44], which are confined to monochromatic operation. Consequently, our platform is intrinsically compatible with modern optical communication technologies like wavelength-division multiplexing (WDM) and mode-division multiplexing (MDM) [65–69]. This offers a compelling prospect for developing high-capacity, short-range wireless optical interconnects, such as chip-to-chip communication [70].

In the realm of optical manipulation, the beams with complex topological textures generated by our device also inspire new research directions. Although direct optomechanical experiments lie outside the scope of this study, the ability to generate micron-scale light fields with controllable spin/orbital angular momentum and multi-wavelength coding in a compact platform could open new avenues for future on-chip optical micromanipulation research, for instance, by using structured light to apply controlled optical forces and torques [71–73]. In our system, the skyrmion density is governed by the spatial scale of the polarization modulation set by the spherulite structure and illumination conditions. Adjusting this scale could, in principle, modify the skyrmion density while maintaining the topology.

In addition to its linear topological structuring capabilities, the unique vortex polarization domain order of this ferroelectric material underpins a second-order nonlinear optical response. We have clearly confirmed that correlated photon pair generation is detected from the spherulite through the SPDC process. Although the nonlinear process, together with the reflection-based design, may render the photon-pair states complex, the tunable topologies make it feasible to engineer target states [74]. Therefore, the significance of generating photon pairs goes beyond being a fundamental property of ferroelectric spherulites; the results may stimulate the research on the topological photon states generation at the quantum level. Future work could focus on the direct generation and observation of correlated skyrmion pairs.

In comparison with metasurface platforms, it is worth noting that, although metasurfaces have enabled achromatic devices such as metalenses and vortex generators, the achromatic generation of optical Skyrmions would be considerably more demanding. Optical Skyrmions require intricate spatial distributions of phase, amplitude, and polarization, imposing substantially higher design complexity than conventional wavefront shaping devices. Moreover, metasurfaces typically rely on sophisticated micro-nano fabrication processes. The discrete nanostructures that compose the metasurface may introduce scattering losses and reduced efficiency, particularly in broadband operation. In contrast, the spherulite-based approach provides a naturally continuous anisotropic medium, offering a feasible route toward broadband achromatic Skyrmion generation.

In conclusion, we have realized an ultra-broadband, tunable optical skyrmion micro-generator using a nanostructured ferroelectric spherulite through crystalization, which overcomes the bandwidth constraints inherent to resonance-based linear and nonlinear light-matter interactions in artificially nanostructured optical systems. Derived from the intrinsic topological landscape of the ferroelectric spherulite, our on-chip photonic platform exploits the synergy between photonic SO coupling and optical focusing, enabling versatile modulation of optical quasiparticles. This work not only demonstrates exceptional optical performances but, more fundamentally, represents a paradigm shift in philosophy, from relying on complex, top-down nano-fabricated artificial structures to harnessing elegant, bottom-up self-assembly processes to create functional photonic devices. Based on such a scheme, it is likely to realize an array of skyrmions with high orders by using arrayed spherulites, in both spatial and temporal domains. We believe that this platform, with its potential for high-performance and multifunctional integration, will profoundly impact the development of next-generation information technologies, particularly in the fields of high-dimensional classical and quantum communications.

4 Methods

4.1 Fabrication of dome-shaped spherulite structure

We dissolved the molecular powder in dichloromethane (2 wt.%) and spin-coated it onto a glass substrate to form a film. Subsequently, the sample was annealed at 130 °C for 5 min using a heating stage (MTI-250). This step resulted in complete melting of the sample and full volatilization of the dichloromethane solvent. After natural cooling to room temperature, a dome-shaped spherulite formed. We utilized a $SiO_2/Ag/SiO_2$ multilayered structure as the substrate for the SPDC characterizations.

4.2 Diffraction simulation

The diffraction processes were simulated using MATLAB. The waist of the input Gaussian beam was matched to the radius of the spherulite. The spherulite was assigned a contact angle of 35°, based on experimental characterization. The incident beam was circularly polarized with a uniform phase distribution. Upon propagation through the dome-shaped spherulite, a circularly polarized state with the reversed handedness emerged, resulting from SO coupling. This SO coupling induces a redistribution of both the phase and intensity between the LCP and RCP components.

We calculated the polarization distribution in the far field using diffraction integral theory under paraxial approximation (Eq. (3–5)). We further deduced the Stokes parameters (Eq. (6–8)) and Skyrme numbers N_{sk} (Eq. (9)) [8].

$$E_{LCP}(x,y,z) = \frac{1}{i\lambda}\iint E_{LCP}(x_0,y_0,z_0)\frac{\exp(ikr)}{r}dx_0dy_0 \tag{3}$$

$$E_{RCP}(x,y,z) = \frac{1}{i\lambda}\iint E_{RCP}(x_0,y_0,z_0)\frac{\exp(ikr)}{r}dx_0dy_0 \tag{4}$$

$$E(x,y,z) = E_{LCP}(x,y,z) + E_{RCP}(x,y,z) \tag{5}$$

$$S_1 = \frac{|E_x|^2 - |E_y|^2}{|E_x|^2 + |E_y|^2} \tag{6}$$

$$S_2 = \frac{2\mathrm{Re}(E_x^*E_y)}{|E_x|^2 + |E_y|^2} \tag{7}$$

$$S_3 = \frac{2\mathrm{Im}(E_x^*E_y)}{|E_x|^2 + |E_y|^2} \tag{8}$$

$$N_{sk} = \frac{1}{4\pi}\iint s\cdot\left(\frac{\partial s}{\partial x}\times\frac{\partial s}{\partial y}\right)dxdy \tag{9}$$

4.3 Full wave simulation

The Stokes textures near the focal plane were simulated using COMSOL Multiphysics 6.1. In the simulation model, the spherulite was assigned a contact angle of 35°, consistent with experimental observations, and a radius of 4.5λ, where λ is the wavelength. The incident beam was configured to exhibit varying polarization ellipticities (see Fig. 4). At the center of the spherulite, the height of the spherulite corresponds to a π phase retardation between the radial and azimuthal polarizations.

4.4 Experimental test of skyrmion texture

The laser source is from a supercontinuum laser (NKT Photonics, SuperK FIU-15) paired with a bandwidth adjustable acousto-optic filter (NKT Photonics, SuperK Varia) to tune the wavelength from 450 to 785 nm. The laser was modulated by a linear polarizer and a continuously variable wave plate (SBC-VIS, Thorlabs) to obtain any polarization sates. The incident beam was focused by a 20× objective (NA 0.4, Olympus) to control the waist at the radius scale of the as-tested spherulite. The dome-shaped spherulite, as a microlens, further focus the incident beam. To collect the optical field near the focal plane of the spherulite, a 40× objective (NA 0.65, Olympus) was used, equipped with a high precision electric translation stage (DDS100, Thorlabs) and a camera in the far field. A pair of waveplate (SAHWP05M-700 or SAQWP05M-1700, Thorlabs) and polarizing beam splitter (GCC-402103, Daheng Optics) before the camera were mounted to extract the left circular (L), right circular (R), horizontal (H), vertical (V), diagonal (D), and anti-diagonal (A) polarization components. Based on the L, R, H, V, D, and A polarization distribution, Stokes parameters of S_1, S_2, and S_3 were deduced (Eq. (10–12)).

$$S_1 = \frac{(I_H - I_V)}{(I_H + I_V)} \tag{10}$$

$$S_2 = \frac{(I_D - I_A)}{(I_D + I_A)} \tag{11}$$

$$S_3 = \frac{(I_L - I_R)}{(I_L + I_R)} \tag{12}$$

4.5 Experimental test of SPDC and SHG

For the SPDC experiment, the micro-photoluminescence setup was based on a confocal microscope equipped with a 3D nanopositioner (Physik Instrumente, P-611.3S) for raster scanning of the sample. Excitation and collection were performed through a single microscope objective (OLYMPUS, LCPLN 100×IR) with a numerical aperture of 0.85. A continuous-wave laser emitting at 785 nm was used for excitation. The laser beam was first filtered by a 1000 nm short-pass filter (Thorlabs, FESH1000) to suppress residual spectral components below 1000 nm before passing through a dichroic long-pass beamsplitter (Thorlabs, DMLP1000R). The generated SPDC signal was filtered by a 1400 nm long-pass filter, coupled into a G652D single-mode fiber, and then directed to a wideband beamsplitter that distributed the signal to SNSPDs (Single Quantum). The detected photon timing signals were analyzed using a low-jitter, streaming time-to-digital converter (Swabian Instruments, Time Tagger Ultra). The time window for the second-order correlation measurement was set to 50 ps.

For the SHG experiment, the fundamental wave light source (1570 nm, 35 fs) with a 1 kHz repetition rate is from a femtosecond optical parametric amplifier (OPerA Solo Integrated OPA, Coherent) for femtosecond laser (Astrella, Coherent) with 800 nm central wavelength. The incident fundamental wave was focused onto the spherulite sample by a 10×objective (PLN10X, NA 0.25, Olympus). The intensity of the incident fundamental wave was recorded by a power meter (PM100D, Thorlabs) equipped with a detector head (S132C, Thorlabs). The generated second-harmonic was filtered by a short-pass filter (FESH0950, Thorlabs). The second-harmonic detection was carried using a spectrometer (HR2000+ES, Ocean Optics).

Supplementary Information

The online version contains supplementary material available at https://doi.org/10.1186/s43593-026-00132-1.

Supplementary Material 1.

Acknowledgements

We acknowledge funding from NSFC (12574458) and the NSFC (Key Grogram Grant No. 52332006), the Postdoctoral Fellowship Program of CPSF (GZC20250073), Singapore Ministry of Education (MOE) AcRF Tier 1 grants (RG157/23 \& RT11/23), Singapore Agency for Science, Technology and Research (A*STAR) MTC Individual Research Grants (M24N7c0080), and Nanyang Assistant Professorship Start Up grant. We thank for Grant No. NRF-CRP30-2023-0003 and NRF-MSG-2023-0002 from the National Research Foundation, and the Dieter Schwarz Foundation through the Endowed Professorship in Quantum Sovereignty and Resilience.

Author contributions

J.S., Y.S., and J. Z. conceived the basic idea behind the work and supervised its development. Y.L. and L.Z. prepared the samples. L.Z., Y.L., H.Z., and X.X. designed the experiments. L.Z., Y.L., and H.Z. performed the experiments. L.Z., Y.L., H.Z., and X.X. analyzed the experimental data. J.S. and Y. L. prepared the first version of the manuscript with input from all authors, J.S and Y.S. supervised the project. All authors took part in discussions, interpreting the results and revising the manuscript.

Funding

National Natural Science Foundation of China, 12574458, Jingbo Sun, National Natural Science Foundation of China, 52332006, Ji Zhou, Postdoctoral Fellowship Program of CPSF, GZC20250073, Yuanfeng Liu, Ministry of Education-Singapore, RG157/23, Yijie Shen, Ministry of Education - Singapore, RT11/23, Yijie Shen, Singapore Agency for Science, Technology and Research (A*STAR) MTC Individual Research Grants, M24N7c0080, Yijie Shen, Nanyang Assistant Professorship Start Up grant, Yijie Shen, National Research Foundation Singapore, NRF-CRP30-2023-0003, Weibo Gao, National Research Foundation Singapore, NRF-MSG-2023-0002, Weibo Gao, Dieter Schwarz Foundation, Weibo Gao.

Data availability

All the data needed to evaluate the conclusions of this work are present in the main text and supplementary materials. The data used in this study are available from the corresponding authors upon reasonable request.

Declarations

Competing interests

The authors declare no competing interests.

Received: 17 December 2025 Revised: 16 March 2026 Accepted: 23 March 2026
Published online: 11 May 2026

References

1. T.H.R. Skyrme, A non-linear field theory. P. Roy. Soc. A **260**, 127 (1961)
2. A. Duzgun, C. Nisoli, Skyrmion spin ice in liquid crystals. Phys. Rev. Lett. **126**, 047801 (2021)
3. J.I. Fukuda, S. Žumer, Quasi-two-dimensional skyrmion lattices in a chiral nematic liquid crystal. Nat. Commun. **2**, 246 (2011)
4. P.J. Ackerman, I.I. Smalyukh, Diversity of knot solitons in liquid crystals manifested by linking of preimages in torons and hopfions. Phys. Rev. X **7**, 011006 (2017)
5. Y. Nahas, S. Prokhorenko, L. Louis, Z. Gui, I. Kornev, L. Bellaiche, Discovery of stable skyrmionic state in ferroelectric nanocomposites. Nat. Commun. **6**, 8542 (2015)
6. F.H. Gong et al., Observation of Néel-skyrmions in bilayered oxide ferroelectrics. Adv. Mater. **37**, 2501411 (2025)

7. M.A.P. Gonalves, M. Paciak, J. Hlinka, Antiskyrmions in ferroelectric barium titanate. Phys. Rev. Lett. **133**, 066802 (2024)
8. N. Nagaosa, Y. Tokura, Topological properties and dynamics of magnetic skyrmions. Nat. Nanotechnol. **8**, 899 (2013)
9. B. Göbel, I. Mertig, O.A. Tretiakov, Beyond skyrmions: review and perspectives of alternative magnetic quasiparticles. Phys. Rep. **895**, 1 (2021)
10. A.C. Balram, U. Wurstbauer, A. Wójs, A. Pinczuk, J.K. Jain, Fractionally charged skyrmions in fractional quantum Hall effect. Nat. Commun. **6**, 8981 (2015)
11. U. Al Khawaja, H. Stoof, Skyrmions in a ferromagnetic Bose–Einstein condensate. Nature **411**, 918 (2001)
12. S. Chen et al., All-electrical skyrmionic magnetic tunnel junction. Nature **627**, 522 (2024)
13. L. Han et al., High-density switchable skyrmion-like polar nanodomains integrated on silicon. Nature **603**, 63 (2022)
14. B.A. Bernevig, C. Felser, H. Beidenkopf, Progress and prospects in magnetic topological materials. Nature **603**, 41 (2022)
15. A.N. Bogdanov, C. Panagopoulos, Physical foundations and basic properties of magnetic skyrmions. Nat. Rev. Phys. **2**, 492 (2020)
16. A.A. Wang et al., Topological protection of optical skyrmions through complex media. Light Sci. Appl. **13**, 314 (2024)
17. J. Chen, A. Forbes, C.W. Qiu, More than just a name? From magnetic to optical skyrmions and the topology of light. Light Sci. Appl. **14**, 28 (2025)
18. X. Lei, Q. Zhan, Topological quasiparticles of light: from spin-orbit coupling to photonic skyrmions. Laser Photonics Rev. **19**, e01427 (2025)
19. C. Cheng, L. Rao, J. Ye, X. Zhao, Z. Che, W. Liu, J. Wang, L. Shi, Navigating optical skyrmions-from historical origins to applications: tutorial. Adv. Opt. Photonics **18**, 1 (2025)
20. Y. Shen, Q. Zhang, P. Shi, L. Du, X. Yuan, A.V. Zayats, Optical skyrmions and other topological quasiparticles of light. Nat. Photonics **18**, 11 (2024)
21. Z. Wan, H. Wang, Q. Liu, X. Fu, Y. Shen, Ultra-degree-of-freedom structured light for ultracapacity information carriers. ACS Photonics **10**, 2149 (2023)
22. Y. Shen, H. Wang, S. Fan, Free-space topological optical textures: tutorial. Adv. Opt. Photon. **17**, 295 (2025)
23. S. Tsesses, E. Ostrovsky, K. Cohen, B. Gjonaj, N.H. Lindner, G. Bartal, Optical skyrmion lattice in evanescent electromagnetic fields. Science **361**, 993 (2018)
24. L. Du, A. Yang, A.V. Zayats, X. Yuan, Deep-subwavelength features of photonic skyrmions in a confined electromagnetic field with orbital angular momentum. Nat. Phys. **15**, 650 (2019)
25. N. Mata-Cervera, D.K. Sharma, Y. Shen, R. Paniagua-Dominguez, M.A. Porras, Skyrmionic polarization texture around the phase singularity of optical vortices. Phys. Rev. Lett. **135**, 033805 (2025)
26. H. Teng, X. Liu, N. Zhang, H. Fan, G. Chen, Q. Cao, J. Zhong, X. Lei, Q. Zhan, Construction of optical spatiotemporal skyrmions. Light Sci. Appl. **14**, 324 (2025)
27. C. Wan, Y. Shen, A. Chong, Q. Zhan, Scalar optical hopfions. eLight **2**, 22 (2022)
28. J. Liu et al., Nanophotonic quantum skyrmions enabled by semiconductor cavity quantum electrodynamics. Nat. Phys. **21**, 1462 (2025)
29. S. Gao, F.C. Speirits, F. Castellucci, S. Franke-Arnold, S.M. Barnett, J.B. Götte, Paraxial skyrmionic beams. Phys. Rev. A **102**, 053513 (2020)
30. W. Lin, Y. Ota, Y. Arakawa, S. Iwamoto, On-chip optical skyrmionic beam generators. Optica **11**, 1588 (2024)
31. Z.L. Deng, T. Shi, A. Krasnok, X. Li, A. Alù, Observation of localized magnetic plasmon skyrmions. Nat. Commun. **13**, 8 (2022)
32. A. Karnieli, S. Tsesses, G. Bartal, A. Arie, Emulating spin transport with nonlinear optics, from high-order skyrmions to the topological Hall effect. Nat. Commun. **12**, 1092 (2021)
33. S. Wang et al., Topological structures of energy flow: Poynting vector skyrmions. Phys. Rev. Lett. **133**, 073802 (2024)
34. M. Cheng, A. Forbes, Research highlight: single photon skyrmions from on-chip quantum dots. eLight **5**, 25 (2025)
35. T.J. Davis, D. Janoschka, P. Dreher, B. Frank, F.J. Meyer zu Heringdorf, H. Giessen, Ultrafast vector imaging of plasmonic skyrmion dynamics with deep subwavelength resolution. Science **368**, eaba6415 (2020)
36. Y. Zeng, Y. Yu, X. Shen, J. Chen, Q. Zhan, Tightly focused optical skyrmions and merons formed by electric-field vectors with prescribed characteristics. Nanophotonics **13**, 251 (2024)
37. Z. Zhang et al., Structured light meets machine intelligence. eLight **5**, 26 (2025)
38. A. Yang et al., Spin-manipulated photonic skyrmion-pair for pico-metric displacement sensing. Adv. Sci. **10**, 2205249 (2023)
39. X. Lei, L. Du, X. Yuan, A.V. Zayats, Optical spin-orbit coupling in the presence of magnetization: photonic skyrmion interaction with magnetic domains. Nanophotonics **10**, 3667 (2021)
40. J. Wu et al., Deep-subwavelength resolution detection of polar magnetization by optical spin meron lattices on hyperbolic metamaterials. Nanophotonics **14**, 4323 (2025)
41. A.A. Wang et al., Perturbation-resilient integer arithmetic using optical skyrmions. Nat. Photonics **19**, 1367 (2025)
42. Y. Shen, Generation of optical skyrmions with tunable topological textures. ACS Photonics **9**, 296 (2022)
43. D. Sugic et al., Particle-like topologies in light. Nat. Commun. **12**, 6785 (2021)
44. T. He et al., Optical skyrmions from metafibers with subwavelength features. Nat. Commun. **15**, 10141 (2024)
45. L. Rao et al., Meron spin textures in momentum space spawning from bound states in the continuum. Phys. Rev. Lett. **135**, 026203 (2025)
46. V. Hakobyan, E. Brasselet, Q-plates: from optical vortices to optical skyrmions. Phys. Rev. Lett. **134**, 083802 (2025)
47. Z. Liu et al., Broadband spin and angle co-multiplexed waveguide-based metasurface for six-channel crosstalk-free holographic projection. eLight **4**, 7 (2024)
48. M. Wang et al., Spin-orbit-locked hyperbolic polariton vortices carrying reconfigurable topological charges. eLight **2**, 12 (2022)
49. W.H. Louisell, A. Yariv, A.E. Siegman, Quantum fluctuations and noise in parametric processes. I. Phys. Rev. **124**, 1646 (1961)
50. S. Friberg, C.K. Hong, L. Mandel, Measurement of time delays in the parametric production of photon pairs. Phys. Rev. Lett. **54**, 2011 (1985)
51. D.C. Burnham, D.L. Weinberg, Observation of simultaneity in parametric production of optical photon pairs. Phys. Rev. Lett. **25**, 84 (1970)
52. C. Couteau, Spontaneous parametric down-conversion. Contemp. Phys. **59**, 291 (2018)
53. H. Zhao et al., Integrated preparation and manipulation of high-dimensional flying structured photons. eLight **4**, 10 (2024)
54. X. Zhao et al., Spontaneous helielectric nematic liquid crystals: electric analog to helimagnets. Proc. Natl. Acad. Sci. U. S. A. **118**, e2111101118 (2021)
55. Y. Shen, Topological bimeronic beams. Opt. Lett. **46**, 3737 (2021)
56. Z. Zhang et al., Topological protection degrees of optical skyrmions and their electrical control. Photonics Res. **13**, B1 (2025)
57. V. Hakobyan, Y. Shen, E. Brasselet, Unitary spin-orbit optical-skyrmionic wave plates. Phys. Rev. Appl. **22**, 054038 (2024)
58. Y. Shen et al., Topologically controlled multiskyrmions in photonic gradient-index lenses. Phys. Rev. Appl. **21**, 024025 (2024)
59. Y. Liu et al., Broadband spin and orbital momentum modulator using self-assembled nanostructures. Adv. Mater. **36**, 2412007 (2024)
60. Y. Liu, L. Zhou, K. Neyts, J. Sun, J. Zhou, Second order optical nonlinearity originated from ferroelectric spherulite with vortex domain. Adv. Opt. Mater. **13**, 2403095 (2025)
61. J. Ma et al., Quantum imaging using spatially entangled photon pairs from a nonlinear metasurface. eLight **5**, 2 (2025)
62. Q. Guo et al., Ultrathin quantum light source with Van der Waals $NbOCl_2$ crystal. Nature **613**, 53 (2023)
63. L. Kallioniemi et al., Van der Waals engineering for quantum-entangled photon generation. Nat. Photonics **19**, 142 (2025)
64. M.B. Rota et al., A source of entangled photons based on a cavity-enhanced and strain-tuned GaAs quantum dot. eLight **4**, 13 (2024)
65. J. Wang et al., Terabit free-space data transmission employing orbital angular momentum multiplexing. Nat. Photonics **6**, 488 (2012)
66. N. Bozinovic et al., Terabit-scale orbital angular momentum mode division multiplexing in fibers. Science **340**, 1545 (2013)
67. L.W. Luo et al., WDM-compatible mode-division multiplexing on a silicon chip. Nat. Commun. **5**, 3069 (2014)
68. Z. Yu et al., A spatial-frequency patching metasurface enabling super-capacity perfect vector vortex beams. eLight **4**, 21 (2024)
69. Z. Jin et al., Phyllotaxis-inspired nanosieves with multiplexed orbital angular momentum. eLight **1**, 5 (2021)
70. B. Wu et al., Chip-to-chip optical multimode communication with universal mode processors. PhotoniX **4**, 37 (2023)

71. L. Paterson, M.P. MacDonald, J. Arlt, W. Sibbett, P.E. Bryant, K. Dholakia, Controlled rotation of optically trapped microscopic particles. Science **292**, 912 (2001)
72. M.E.J. Friese, T.A. Nieminen, N.R. Heckenberg, H. Rubinsztein-Dunlop, Optical alignment and spinning of laser-trapped microscopic particles. Nature **394**, 348 (1998)
73. X. Xie, Y. Shen, Topological light manipulating particles: a perspective. Light Manip. Appl. **1**, 202501 (2026)
74. C. Li et al., Arbitrarily structured quantum emission with a multifunctional metalens. eLight **3**, 19 (2023)